

# Non-Fermi liquid behavior below the Néel temperature in the frustrated heavy fermion magnet $\text{UAu}_2$

Christopher D. O'Neill<sup>a,b,1</sup>, Julian L. Schmehr<sup>a,b</sup>, Harry D. J. Keen<sup>a,b</sup>, Luke Pritchard Cairns<sup>a,b</sup>, Dmitry A. Sokolov<sup>a,b</sup>, Andreas Hermann<sup>a,b</sup>, Didier Wermeille<sup>c</sup>, Pascal Manuel<sup>d</sup>, Frank Krüger<sup>d,e</sup>, and Andrew D. Huxley<sup>a,b,1</sup>

<sup>a</sup>School of Physics and Astronomy, University of Edinburgh, Edinburgh EH9 3FD, United Kingdom; <sup>b</sup>Centre for Science at Extreme Conditions, University of Edinburgh, Edinburgh EH9 3FD, United Kingdom; <sup>c</sup>The UK Materials Science Facility, European Synchrotron Radiation Facility, F-38043 Grenoble, France; <sup>d</sup>ISIS Pulsed Neutron and Muon Source, Science Technology Facilities Council Rutherford Appleton Laboratory, Oxon OX11 0QX, United Kingdom; and <sup>e</sup>London Centre for Nanotechnology, University College London, London WC1H 0AH, United Kingdom

Edited by Zachary Fisk, University of California, Irvine, CA, and approved October 27, 2021 (received for review February 10, 2021)

The term Fermi liquid is almost synonymous with the metallic state. The association is known to break down at quantum critical points (QCPs), but these require precise values of tuning parameters, such as pressure and applied magnetic field, to exactly suppress a continuous phase transition temperature to the absolute zero. Three-dimensional non-Fermi liquid states, apart from superconductivity, that are unshackled from a QCP are much rarer and are not currently well understood. Here, we report that the triangular lattice system uranium diauride ( $\text{UAu}_2$ ) forms such a state with a non-Fermi liquid low-temperature heat capacity  $C/T \sim \log(1/T)$  and electrical resistivity  $\rho(T) - \rho(0) \propto T^{1.35}$  far below its Néel temperature. The magnetic order itself has a novel structure and is accompanied by weak charge modulation that is not simply due to magnetostriction. The charge modulation continues to grow in amplitude with decreasing temperature, suggesting that charge degrees of freedom play an important role in the non-Fermi liquid behavior. In contrast with QCPs, the heat capacity and resistivity we find are unusually resilient in magnetic field. Our results suggest that a combination of magnetic frustration and Kondo physics may result in the emergence of this novel state.

non-Fermi liquid | quantum criticality | Kondo physics | magnetic frustration | charge density wave

The understanding of metals and superconductors rests on the paradigm that their low-energy excitations are governed by quasiparticle excitations around a stable Fermi surface. This paradigm breaks down at quantum critical points (QCPs) in a metal (1, 2), where the emergent spatial- and temporal-scale invariance results in spectral functions that no longer exhibit quasiparticle poles. As the temperature is increased, a region opens up about a QCP in which various quantities, such as the heat capacity and electrical resistivity, change with temperature in different ways from a Fermi liquid. A prominent example of such a non-Fermi liquid (NFL) is the “strange metal” in the copper-oxide superconductors (3), which has a  $T$ -linear resistivity instead of a leading  $T^2$  dependence characteristic of a Fermi liquid. A QCP is in this case hidden under a superconducting dome (4). Very recently, angle-resolved photoemission spectroscopy in the high- $T_c$  cuprate family  $\text{Bi}2212$  has challenged this picture. It revealed an abrupt recovery of quasiparticles above a temperature-independent doping level (5) coinciding with the discontinuous vanishing of the pseudogap. This suggests that the strange metal might not emerge from a QCP but could instead be a distinct NFL state of matter, and this begs the question as to whether such states occur more widely.

Itinerant magnets and heavy-fermion metals exhibit QCPs and NFLs that are easier to study than the copper oxides owing to lower characteristic temperatures and the ease with which they can be tuned with pressure and magnetic fields (6). However, very few NFL states (not counting superconductivity) have been found that do not emanate from a QCP (1, 7). One rare example occurs in the high-pressure partially ordered phase of

the helimagnet  $\text{MnSi}$ . It is stable over a wide pressure range and has a  $T^{3/2}$  electrical resistivity power law below  $\sim 6$  K down to millikelvin temperatures (8, 9). The presence of a large topological Hall signal suggests that a partially ordered magnetic structure with nontrivial topology may underlie the NFL (10, 11).

$\beta\text{-YbAlB}_4$  is magnetically unordered and provides an example of NFL behavior without tuning in zero field. This NFL may be the result of a very unusual QCP at exactly zero field or instead, represent a unique quantum critical phase that is driven into a Fermi liquid state by an infinitesimal magnetic field (12). However, resistivity measurements have indicated that the NFL may still be attached to a QCP that can be reached with pressure (13).

There are two well-known theoretical ways to get a three-dimensional (3D) NFL not emanating from QCPs, both based on local physics. The first is the two-channel Kondo effect, requiring an exact balance between two screening channels (14), that like a QCP, could be thought of as a point of precise tuning. NFL behavior for the two-channel Kondo model has recently been seen above quadrupole ordering temperatures in a series of cubic Pr materials with non-Kramers doublet ground states (15) and in related dilute systems with small concentrations of Pr replacing Y (16), as well as in earlier studies of  $\text{Y}_{1-x}\text{U}_x\text{Pd}_3$  (17). These local NFLs are predicted to have a temperature dependence of

## Significance

In metals, identical Fermions in three dimensions invariably form a Fermi liquid or superconducting state at low temperature, except at quantum critical points separating differently ordered states. We report that uranium diauride ( $\text{UAu}_2$ ) breaks this paradigm, hosting a robust non-Fermi liquid within a magnetically ordered state. Non-Fermi liquid behavior untethered from a quantum critical point in a clean metal has only clearly been seen in the magnetically partial-ordered phase of  $\text{MnSi}$  at high pressure and the potential quantum critical phase of magnetically unordered  $\beta\text{-YbAlB}_4$ . Unlike  $\text{MnSi}$  and  $\beta\text{-YbAlB}_4$ ,  $\text{UAu}_2$  is magnetically ordered, so the mechanism in this case is different, suggesting such states may exist more widely. An accompanying charge density wave suggests this mechanism may involve charge degrees of freedom.

Author contributions: C.D.O.N., J.L.S., F.K., and A.D.H. designed research; C.D.O.N., J.L.S., H.D.J.K., L.P.C., D.A.S., A.H., D.W., P.M., F.K., and A.D.H. performed research; C.D.O.N., J.L.S., H.D.J.K., L.P.C., A.H., D.W., P.M., F.K., and A.D.H. analyzed data; and C.D.O.N., F.K., and A.D.H. wrote the paper.

The authors declare no competing interest.

This article is a PNAS Direct Submission.

Published under the PNAS license.

<sup>1</sup>To whom correspondence may be addressed. Email: Chris.O'Neill@ed.ac.uk or a.huxley@ed.ac.uk.

This article contains supporting information online at <https://www.pnas.org/lookup/suppl/doi:10.1073/pnas.2102687118/-DCSupplemental>.

Published December 3, 2021.

their electrical resistivity  $\rho(T) - \rho(0) \propto \sqrt{T}$  and be sensitive to magnetic field (18). The second way requires a range of single-channel Kondo energy scales extending to zero energy, generated by disorder (19), and results in an approximately  $T$ -linear resistivity. The NFL state we report in  $\text{UAu}_2$  is robust over a wide range of magnetic fields and has signatures that are too strong to be attributed to impurities.  $\text{UAu}_2$  is also crystallographically well ordered with a low residual electrical resistivity, ruling out explanations based solely on chemical disorder. We also do not see the entropy release in magnetic field that would be expected for the usual two-channel Kondo effect.

For  $\text{MnSi}$ , reported thermodynamic measurements in the NFL state at high pressure are restricted to the lattice constant (20, 21). The measurements show that the thermal expansion has a low temperature dependence  $\alpha \propto T$  (20), which follows the same power law as a conventional Fermi-liquid. Here, the NFL we report in  $\text{UAu}_2$  is manifest in thermodynamic measurements extending to very low temperature, and unlike for  $\beta\text{-YbAlB}_4$ , this is in a fully magnetically ordered state.

$\text{UAu}_2$  is a little-studied heavy fermion metal known to order magnetically at 43 K (22). It has a simple  $\text{AlB}_2$ -type hexagonal crystal structure (23) comprising a vertical stacking of flat sheets of a triangular lattice of U atoms, separated by sheets of gold atoms (Fig. 1A). The calculated paramagnetic band structure is shown in Fig. 1B (calculation details and band dispersions are given in the *SI Appendix*). The magnetic phase diagram and magnetic structure we find are shown in Fig. 1C. After discussing magnetic and charge ordering (Fig. 2), we present our thermodynamic and transport measurements showing NFL behavior (Figs. 3 to 5), and then, we discuss these and present our conclusions.

## Magnetic Phase Diagram and Charge Order

Theoretically, a two-dimensional (2D) triangular lattice with only nearest neighbor antiferromagnetic interactions adopts three-site order defined by the moment direction on three nearest neighbor sites. The magnetic unit cell then has dimensions  $\sqrt{3} \times \sqrt{3}$  compared with the atomic cell (24) (Fig. 1A). For an Ising magnet, where the moments are constrained to be parallel or antiparallel to a fixed direction, it is impossible to align adjacent moments on the three sites antiparallel, leading to the phenomena of geometric frustration with a ground-state degeneracy that depends exponentially on the system size, giving a finite ground-state entropy per volume. The inclusion of higher than quadratic-order spin fluctuations in the antiferromagnetic Ising–Heisenberg model (25) or of interactions that have a range beyond nearest neighbor (26) lifts this degeneracy. The low-temperature state is then predicted to be ferrimagnetic with spins on the three nearest neighbor sites  $\{\uparrow, \uparrow, \downarrow\}$  (27, 28). A partially ordered  $\{\uparrow, \downarrow, 0\}$  state may occur at higher temperature where higher-entropy states are favored (29). In  $\text{UAu}_2$ , the triangular lattice is stacked along the third direction, forming columns of U atoms. Isostructural materials are known to exhibit a wide range of complex magnetic structures (30).

We performed elastic neutron scattering measurements on a finely powdered sample and individual single crystals from two Czochralski growths to determine the magnetic order in  $\text{UAu}_2$ . The experimentally determined temperature–magnetic field phase diagram for field  $H \parallel c$  is shown in Fig. 1C. At low temperature (2 K), a magnetic field above 6 T (along the  $c$  axis) induces a strongly polarized commensurate  $\sqrt{3} \times \sqrt{3}$  state with

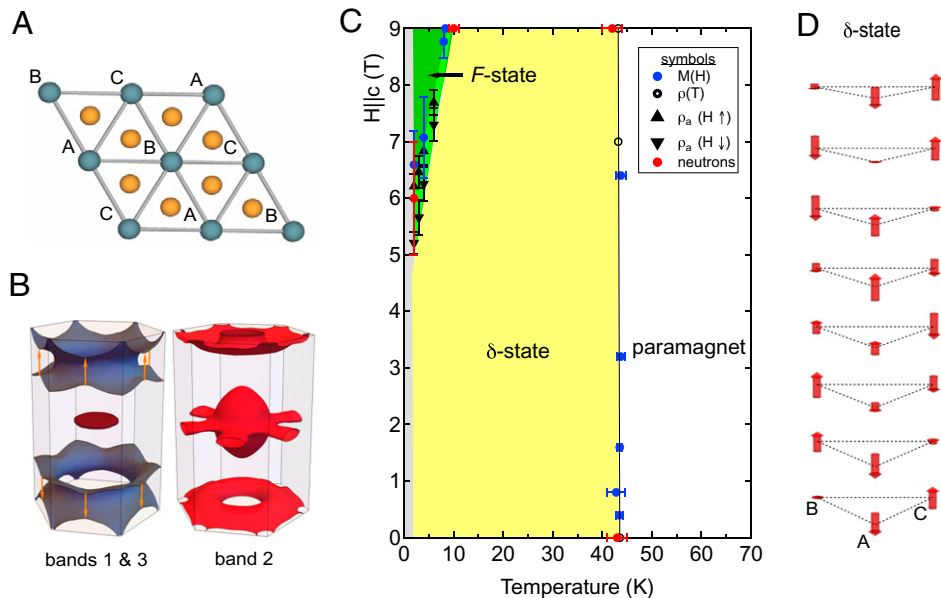


**Fig. 1.** (A) The crystal structure of  $\text{UAu}_2$  viewed along the  $c$  axis showing  $2 \times 2$  unit cells in the  $ab$  plane. Au atoms (colored gold) are at  $c = 1/2$ , and U atoms (blue) are at  $c = 0$ . There is only a single crystallographic inequivalent site for each atom. The U atoms lie on a triangular lattice in the plane. In the magnetic unit cell, U atoms in the plane labeled A, B, and C are no longer equivalent to each other. Geometric frustration occurs for Ising moments with antiferromagnetic nearest neighbor interactions. To see this, consider the case where the A sites have spin  $\uparrow$  and C sites have spin  $\downarrow$ ; the energy is then the same for either choice of spin direction at every B site. (B) The calculated Fermi surface. The “crown” in blue is a hole band (band 1), and the “button” (maroon) is an electron band (band 3). Band 2 has two electron pockets: the “propeller” at the zone center and the “doughnut” at the zone edge. The orange arrows connecting menisci of the crown are nesting vectors  $(0, 0, 0.14)$  responsible for a peak in the static Lindhard function. Band dispersions and the density of states, decomposed into orbital contributions, are shown in *SI Appendix, Fig. S1*. (C) The temperature–magnetic field phase diagram determined from our measurements of intermediate- and high-quality single crystals. The transitions are detected in magnetization measurements ( $M$ ) and resistivity ( $\rho$ ) and with neutron scattering (*SI Appendix* has details). In the ferrimagnetic state ( $F$  state),  $A = \uparrow$ ,  $B = \downarrow$ , and  $C$  is aligned with the magnetic field with no modulation along the  $c$  axis. The ordered state that occupies most of the figure is incommensurately modulated along the  $c$  direction ( $\delta$  state). This magnetic structure is shown in *D*, which depicts seven–unit cell lengths along the  $c$  direction (vertical). The moments (red arrows) are  $\vec{m} \propto \vec{c} \cos(2\pi\delta \cdot z + \theta)$ . The phase angle  $\theta$  differs by  $\pm 2\pi/3$  between adjacent columns. In the region labeled  $\delta$  state, a small trace of the  $F$  state was still found. For high-quality crystals, the corresponding volume fraction was below 0.6%.

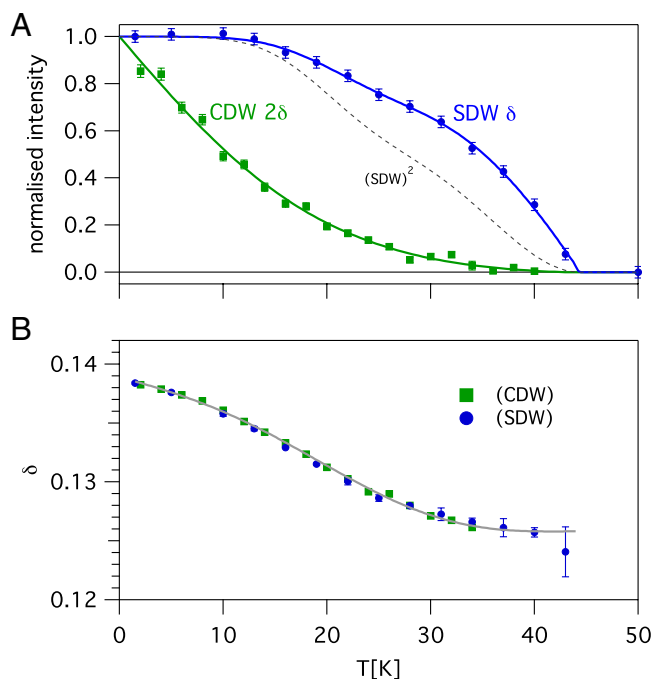


**Fig. 2.** (A) The zero-field temperature dependence of the SDW and CDW amplitudes squared, normalized to their values at low temperature proportional to the integrated neutron and X-ray scattering at Bragg peaks with modulation vectors  $\delta$  (neutrons, SDW) and  $2\delta$  (X-rays, CDW). Both neutron and X-ray measurements were performed on the same high-quality single crystals that contained less than 0.6% of the  $F$  state (SI Appendix). The lines through the points are guides to the eye. The SDW amplitude clearly saturates at low temperatures below 15 K and has a globally convex shape, which are conventional features. In contrast, the CDW amplitude continues to grow with decreasing temperature at the lowest temperatures and has a concave shape. The dashed line shows the square of the SDW intensity, which is the expected form for a charge modulation due to magnetostriction. The CDW in  $\text{UAu}_2$  clearly has a very different temperature dependence, showing that it is not principally caused by magnetostriction. B shows that the value of  $\delta$  is the same for both the CDW and SDW (the line is a guide to the eye).

Bragg peaks at  $(\frac{1}{3}, \frac{1}{3}, 0)$  (reflection indices are given relative to the crystal structure). This state is identified as the ferrimagnetic state  $\{\uparrow, \uparrow, \downarrow\}$  with no modulation along the columns (hereon referred to as the  $F$  state). The ordered uranium moments have magnitude  $\sim 1.0 \mu_B$ , deduced from magnetometer measurements and the neutron data. In the rest of this work, we focus on the  $\delta$  state present at lower fields. This state exists alongside a residual fraction of  $F$  state. For high-quality single crystals, the volume fraction of  $F$  state at zero field is less than  $\sim 0.6\%$  over the complete temperature range studied. A more significant volume fraction of powdered and polycrystalline samples transforms to the  $F$  state at low temperature in zero applied field, most likely as a result of internal strain. A comprehensive description of the fraction of  $F$  state and sample quality is provided in the SI Appendix.

The  $\delta$  state is a  $\sqrt{3} \times \sqrt{3}$  magnetic state that is sinusoidally modulated along the  $c$  direction with magnetic Bragg reflections at  $(\frac{1}{3}, \frac{1}{3}, \delta)$ . The modulation period  $\delta$  is incommensurate with the lattice, and it changes continuously from  $\delta \sim 1/8$  at  $T_N$  to  $\delta \sim 0.138$  at 2 K (Fig. 2B) and is insensitive to the magnetic field along  $c$ . The magnetic moments are aligned with the  $c$  axis (SI Appendix). This is consistent with the magnetic susceptibility, which shows a much more pronounced kink at  $T_N$  in the  $c$ -axis component than for the  $a$ -axis (SI Appendix, Fig. S6), and the near-vertical transition line between the  $\delta$  state and paramagnetic state in the magnetic field temperature phase diagram (Fig. 1C). The magnetic moments on the three sites in a triangle have to

sum to zero at all temperatures in the  $\delta$  state since any ferrimagnetic component would lead to additional reflections such as  $(1, 0, \delta)$ , where no intensity was seen.

States consistent with the above observations can be built from any combination of two states, one with the phase of the modulation differing by  $2\pi/3$  between neighboring columns  $A \rightarrow B \rightarrow C$  (Fig. 1D) denoted  $\delta_+$  and the other with phase differences of  $-2\pi/3$  denoted  $\delta_-$ . The transition from  $\delta$  to  $F$  induced by an applied field is strongly first order (hysteretic) and accompanied by a sharp drop in the electrical resistivity (SI Appendix, Fig. S7). The  $\delta$  state in  $\text{UAu}_2$  is similar to the magnetic state observed below  $T_N$  in the rhombohedral insulator  $\text{Ca}_3\text{Co}_2\text{O}_6$  (31). However, at lower temperature, the magnetic structure in  $\text{Ca}_3\text{Co}_2\text{O}_6$  transforms slowly to an antiferromagnetic striped state that no longer preserves the  $\sqrt{3} \times \sqrt{3}$  arrangement (32).

We performed zero-field X-ray scattering measurements on the same single crystals studied with neutrons. Resonant scattering at the U  $M_4$  edge identified the same magnetic peaks seen with neutrons in the  $\delta$  state, and azimuthal scans with polarization analysis confirmed the moments are directed along the  $c$  axis. We also made measurements with 11.2-keV X-ray photons and a much higher X-ray intensity. These measurements revealed the presence of charge peaks below  $T_N$  at  $(\frac{1}{3}, \frac{1}{3}, 2\delta)$  and equivalent positions. The identical temperature dependence of  $\delta(T)$  for the charge density modulation (charge density wave [CDW]) and the magnetic modulation (spin density wave [SDW]) shows they are related (Fig. 2B). A careful search was made at 2 K and close to  $T_N$  for diffraction peaks at  $(\frac{1}{3}, \frac{1}{3}, 0)$  and related positions; none were found. Given that the CDW is linked to the magnetic structure, peaks at these positions would be expected for magnetic states made from superpositions of opposite helicity  $\delta_+$  and  $\delta_-$ . The absence of these peaks, therefore, implies that locally the  $\delta$  state is pure  $\delta_+$  or  $\delta_-$  at both temperatures. This rules out an entropy-driven transformation to a partially ordered state. To see if we could understand the origin of the magnetic  $\delta$  structure, we examined a simple theoretical model with fixed Ising moments. For long-range exchange parameters along the  $c$ -axis that fix the period of the modulation and a weak nearest neighbor antiferromagnetic exchange in the plane, we confirmed that the spin arrangement observed experimentally and shown in Fig. 1D minimizes the free energy (SI Appendix). The modulation along the  $c$ -axis may result from nesting features of the Fermi surfaces (Fig. 1B).

We found no evidence for higher harmonics of the SDW or CDW order that would accompany a squaring up of the modulation in either the neutron or X-ray studies (SI Appendix, Figs. S9 and S11). The temperature dependence of the intensity of the SDW and CDW is shown in Fig. 2A. A CDW at  $q = 2\delta$  can be induced by magnetostriction, as found for the SDW in chromium (33), with charge peak intensities proportional to the square of the magnetic intensities and with additional higher multiple CDW harmonics at  $q = 2n\delta$  (for integer  $n$ ). In contrast, the temperature dependence of the CDW for  $\text{UAu}_2$  is not a simple power of the magnetic intensity  $I_{\text{SDW}}$  (Fig. 2A), and there are no higher harmonics. While the magnetic intensity changes very little below  $T^* \sim 15$  K, the intensity of the CDW in  $\text{UAu}_2$  increases strongly as the temperature is reduced below  $T^*$ , with a strong temperature dependence down to the lowest temperature measured (2 K). Combined CDW/SDW order with a charge modulation vector that is twice the magnetic modulation vector has also been reported in stripe phases (34) in cuprate superconductors and closely related nickelates. In these systems, rivers of high charge density act as antiphase domain boundaries between antiferromagnetic regions. However, unlike in  $\text{UAu}_2$ , the charge ordering is always observed at a higher temperature than the magnetic ordering, characteristic of a transition that is driven by charge (34). For  $\text{UAu}_2$ , the CDW develops below the magnetic ordering temperature, suggesting it has a different origin from

the cuprates. The strong low-temperature dependence suggests the CDW may be linked with the NFL behavior that we describe next.

### Thermodynamic and Transport Measurements

We find that the heat capacity has an NFL behavior  $C/T = A \log(\Theta/T)$  with  $A = 68 \text{ mJ mol}^{-1} \text{ K}^{-2}$  and  $\Theta = 69 \text{ K}$  (Fig. 3A) over at least a decade in temperature below 4 K. Other contributions, including from phonons, make it difficult to determine an upper limit above 4 K. A natural temperature scale over which this behavior might persist is deduced from the  $c$ -axis resistivity, which shows a decrease in slope in the range from 10 to 20 K (Fig. 3C) and the susceptibility that starts to increase with decreasing temperature in the same temperature range (Fig. 3B). The change in entropy due to the  $\log(\Theta/T)$  term between 0 and 20 K equates to  $0.5R \log(2)$  per uranium. The low-temperature differential susceptibility in the  $\delta$  state follows  $\chi(0) - \chi(T) \propto \log T$  (Fig. 3B). The ratio of the coefficients of the  $\log(T)$  terms

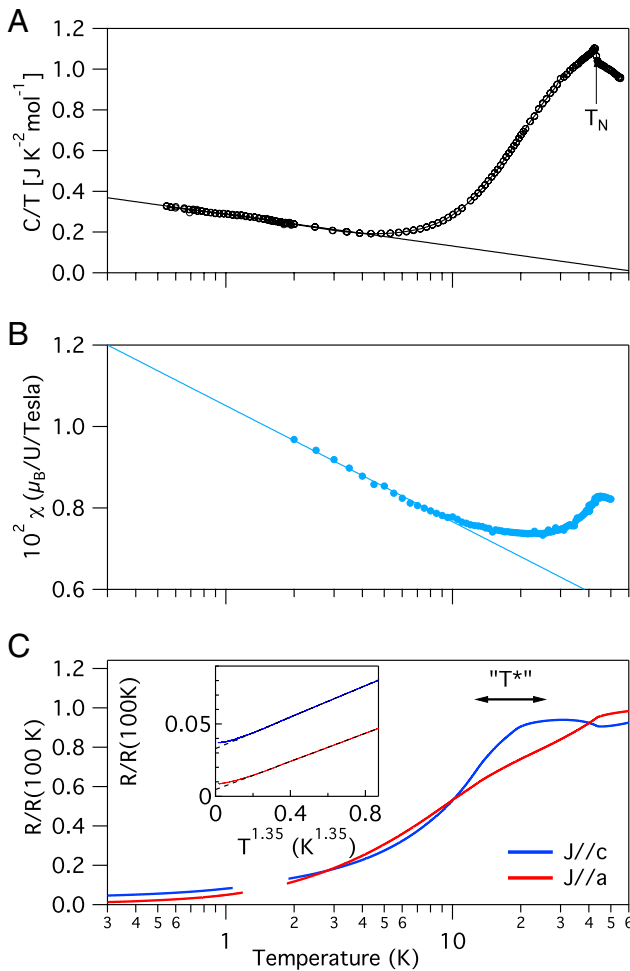


**Fig. 3.** Low-temperature macroscopic properties of UAu<sub>2</sub> in zero field. A–C show (A) the heat capacity divided by temperature  $C/T$ , (B) the susceptibility  $\chi$ , and (C) the resistivity  $\rho$  plotted against temperature on a logarithmic scale. There are clear signatures at the magnetic ordering temperature  $T_N = 43 \text{ K}$  and a cross-over in behavior around  $T^* \approx 20 \text{ K}$ . In A, the solid line shows a fit to  $A - B \log(T)$  between 0.5 and 4 K. In B, the solid line is a fit to  $A - B \log(T)$  for  $T < 9 \text{ K}$ . In C, the resistivity is normalized to the value at 100 K. Inset shows the low-temperature resistivity against  $T^{1.35}$ . The straight dashed lines indicate that the  $T^{1.35}$  dependence persists to  $\sim 300 \text{ mK}$ . A gradual increase in the exponent of resistivity to  $T^2$  occurs below 300 mK. All measurements were performed on high-quality single crystals that contain less than 0.6% of the  $F$  state (SI Appendix).

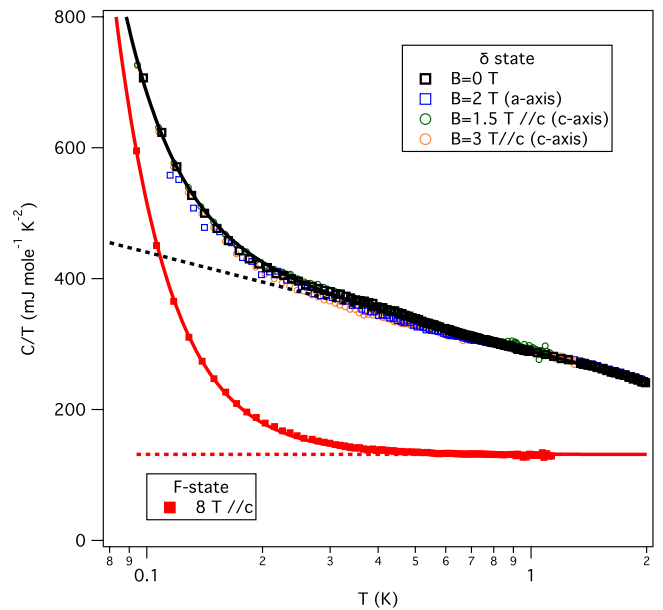


**Fig. 4.** Temperature dependence of the heat capacity divided by temperature for high-quality single crystals of UAu<sub>2</sub> at low temperature. There is only a very weak magnetic field dependence of the heat capacity for fields of a few teslas in this temperature range, where the sample is in the  $\delta$  state. The solid line (black) is a fit at zero field to  $C/T = a/T^3 + b - c \log(T)$  ( $a$ ,  $b$ , and  $c$  are constants). The first term in this expression arises from the nuclear hyperfine states of gold and uranium nuclei (SI Appendix has details). The dashed line (black) shows the electronic contribution from the other two terms. A  $\log(T)$  behavior is characteristic of an NFL. For a field  $H \parallel c = 8 \text{ T}$ , the sample is transformed into the commensurate ferrimagnetic  $F$  state (the high-quality single crystals studied here have less than 0.6% of the  $F$  state present in the  $\delta$ -phase) (SI Appendix). The temperature dependence in this case is  $C/T = a'/T^3 + b'$  (red solid line). There is no  $\log(T)$  term, and the electronic contribution is constant (red dashed line), characteristic of a normal Fermi liquid. For intermediate  $c$ -axis fields, the sample transforms abruptly and hysteretically between the two states. Some crystals have an additional bump in  $C/T$  of height less than  $20 \text{ mJ mol}^{-1} \text{ K}^{-2}$  located in the temperature range from 300 to 500 mK with a sample-dependent width (SI Appendix, Fig. S3). The bump is suppressed with field and absent in fields of several teslas. The sample dependence of this feature suggests that it has an extrinsic origin (SI Appendix). It makes an insignificant contribution to the entropy compared with the  $\log(T)$  term.

for  $C/T$  (in units of  $\text{joule kelvin}^{-2} \text{ mole}^{-1}$ ) and  $\chi$  (in units of  $\mu_B$  per tesla) is close to the Wilson ratio  $(\pi^2/3)(Rk_B/\mu_B)$ . The NFL behavior is, therefore, consistent with a renormalization of the quasiparticle effective mass. This contrasts with the case of  $\beta\text{-YbAlB}_4$ , where the Wilson ratio diverges toward low temperature, consistent with strong and increasing ferromagnetic fluctuations with decreasing temperature (12).

The heat capacity measured at very low temperature is shown in Fig. 4. Gold nuclei have an extremely small dipole moment but significant quadrupole moment. This leads to a  $C/T \sim 1/T^3$  quadrupolar Schottky contribution to  $C/T$  that dominates the heat capacity below  $\sim 0.1 \text{ K}$ . The electric field gradient at the gold site was calculated from the band structure and splits the gold nuclear levels into two doublets separated by  $\Delta E/k_B \sim 9 \text{ mK}$ . There is additionally a small contribution from <sup>235</sup>U (the depleted uranium in our samples contains  $\sim 0.2\%$  <sup>235</sup>U), which also has a quadrupole moment. The observed magnitude of the  $1/T^3$  coefficient may be fully accounted for by these terms (SI Appendix has details). The strong Ising anisotropy of UAu<sub>2</sub> would mean any transverse spin-wave fluctuations are gapped, and therefore, no  $T^3$  contribution from magnons is expected.

As well as the  $\log(T)$  term and nuclear Schottky contribution in zero magnetic field, in some crystals there is a weak

additional contribution to the heat capacity below 500 mK (*SI Appendix, Fig. S3*) associated with only a very tiny change of entropy [ $\sim 0.02R \log(2)$ ]. Unlike the  $\log(T)$  term, this extra contribution is suppressed in a small magnetic field and is attributed to defects (*SI Appendix, Fig. S3*). No change in the magnetic Bragg peak intensity or modulation vector was seen in the  $\delta$  state between 1 K and 40 mK with neutron scattering, shown in *SI Appendix, Fig. S10*; therefore, we can rule out any bulk magnetic transition at low temperature and zero field.

$C/T = A \log(\Theta/T)$  has only a very weak field dependence in fields of up to several teslas, shown in Fig. 4. In field, after removing the  $1/T^3$  contribution,  $C/T \sim \log(1/T)$  appears to persist to the lowest temperature for which the Schottky term can be reliably subtracted  $\sim 0.1$  K (*SI Appendix, Fig. S15*). For larger fields along  $c$ , above 4 T, the  $\delta$  state can be obtained by zero-field cooling, but it is metastable and transits to the  $F$  state abruptly and irreversibly as the temperature is increased. At 8 T, the sample is in the  $F$  state irrespective of the field history, and  $C/T = \gamma$  is a constant, characteristic of a standard Fermi liquid (plus a  $1/T^3$  nuclear Schottky contribution). Thus, in summary, the  $\delta$  state has an electronic heat capacity  $C/T \sim \log(1/T)$  dependence from  $\sim 0.1$  to above 4 K that survives in magnetic fields of several teslas.

The thermal expansion determined from the X-ray scattering measurements is shown in Fig. 5, where it is compared with that calculated from  $C/T$  and a temperature-independent Grüneisen parameter,  $\Gamma$ . The consistency of the two curves below 10 K does not suggest any low-temperature divergence of  $\Gamma$ .

We will now discuss the electrical resistivity. The low-temperature resistivity of  $\text{UAu}_2$  has an NFL  $\rho(T) - \rho(0) \propto T^{1.35}$  dependence down to a temperature below  $\sim 300$  mK (Fig. 3 C, *Inset*). Below this temperature, there is a gradual increase in exponent that at the very lowest temperatures can be described by  $\rho(T) - \rho(0) \propto T^2$ , the expected dependence for a correlated Fermi liquid. This may indicate that the energy scale for intersite coherence is 200 – 400 mK, or it may be a cross-over to another lower-temperature regime. Analogous to the heat capacity, the NFL behavior and the cross-over temperature in resistivity are insensitive to magnetic field in the  $\delta$  state (*SI Appendix, Fig. S8*). The resistivity is distinctly

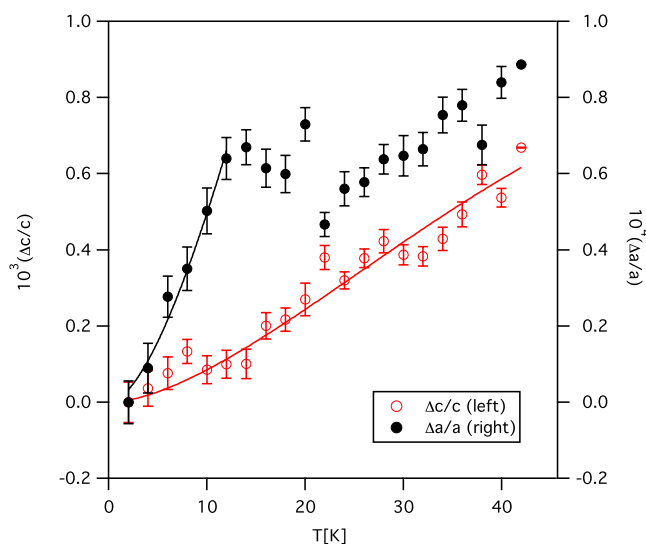


**Fig. 5.** The relative change in the  $a$  and  $c$  lattice parameter as a function of temperature in zero field deduced from X-ray diffraction for the  $(3,0,0)$  and  $(3,0,1)$  diffraction peaks of high-quality single crystals that contain less than 0.6% of the  $F$  state. The solid lines are fits to  $\Delta a \propto \Delta c \propto \int C(T)dT$ , with  $C/T \sim \log(69/T)$  (the only free parameter is a constant of proportionality for each direction). This analysis is valid for a constant Grüneisen parameter.

different from that in the NFL of the partially ordered phase of  $\text{MnSi}$ , where the  $T^{3/2}$  dependence exists to a much lower temperature (8, 9). Based on the cross-over in the resistivity, the  $\log(T)$  term in  $C/T$  might also be expected to saturate at a low temperature below 300 mK. The analysis of  $C/T$  below 300 mK depends on the accurate subtraction of the  $1/T^3$  tail from the nuclear Schottky contributions. A modification of the nuclear contribution could potentially obscure the identification of such a saturation.

## Discussion

We now discuss possible explanations of our findings. In a metal, uranium usually has a valence somewhere between  $\text{U}^{4+}$  (electron configuration  $5f^2$ ) and  $\text{U}^{3+}$  ( $5f^3$ ). Crystal symmetry imposes that the lowest states of the former configuration have total angular momentum quantum number  $J = 4$  and are split into three non-Kramers doublets and three singlets (35). The non-Kramers doublets have a quadrupole moment but can additionally carry a dipole moment. The lowest-energy states for  $\text{U}^{3+}$  have  $J = 9/2$  and are split by the crystal field into five Kramers doublets. The heat capacity in Fig. 2 would be exceeded if there was a Schottky contribution from the crystalline electric field (CEF) levels with a lowest-level splitting less than  $\sim 40$  K or a phonon term with a Debye temperature below  $\sim 170$  K. It is, however, possible to accommodate within the measured heat capacity a Schottky term with a larger splitting as might arise from the CEF acting on U moments (and a larger Debye temperature). These contributions to the heat capacity are insignificant below  $\sim 4$  K, where  $C/T \sim \log(1/T)$  is observed.

We now turn to discuss the origin of  $C/T \sim \log(1/T)$ ; this particular dependence is referred to with the abbreviation MFL (marginal Fermi liquid) in the following. Although a rigid density of states with a 2D Van Hove singularity can give  $C/T \sim \log(1/T)$ , this cannot account for the magnitude of the constant of proportionality observed and would be sensitive to magnetic field.

An explanation based on the proximity to a QCP between the  $\delta$  state and high-field  $F$  state can be ruled out; the field-induced transition is strongly first order, whereas a continuous transition is required for a QCP. Additionally, approaching the  $\delta - F$  transition with an increasing magnetic field does not lead to strengthening of the  $\log(T)$  term in the heat capacity, an enhancement of the zero temperature  $T^2$  contribution in the resistivity, or a lowering of the cross-over temperature to  $T^{1.35}$  (*SI Appendix, Fig. S8*), all of which would be expected approaching a quantum critical transition.

For magnetically unordered ground states, standard explanations for an MFL are based on a proximity to a magnetic QCP. Considering only magnetic degrees of freedom, an MFL is found for Hertz–Millis QCPs (36) between paramagnetism and either 3D ferromagnetism or 2D antiferromagnetism (37). The key point is that this is restricted to temperatures above  $T_N$ . Below  $T_N$ , the magnetic fluctuations linked to the order cannot give rise to quantum critical behavior since the fermion spectrum is gapped at the ordering vector, and the only excitations within this gap are Goldstone modes that are undamped and cannot give the required divergence of the self-energy (38). Thus, while there are many magnetically unordered materials that are MFLs,  $\text{UAu}_2$  provides a unique example where such a behavior is found within a magnetically ordered state. A different degree of freedom is, therefore, required to explain NFL behavior below  $T_N$ .

Quadrupole order, linked to a non-Kramers  $\text{U}^{4+}$  doublet single-ion ground state, provides a natural candidate for a second degree of freedom. One possibility is that this degree of freedom is close to ordering at a QCP below  $T_N$ .  $\text{Ce}_3\text{Pd}_{20}\text{Si}_6$  provides an example of the opposite case, where an antiferromagnetic QCP occurs within a quadrupolar-ordered state (39, 40). A proximity

to a QCP can, however, be ruled out for  $\text{UAu}_2$  from the thermal expansion below 10 K, shown in Fig. 5. Below 10 K, the thermal expansion is proportional to the heat capacity, corresponding to a temperature-independent Grüneisen parameter  $\Gamma$ . This contrasts sharply with a divergence of  $\Gamma$  that would be expected approaching a QCP. The same conclusion also applies to QCPs from extensions (41) of the Doniach phase diagram (42) or for a quantum critical valence transition (43). While we have ruled out a QCP, the nonmonotonic variation of the thermal expansion  $\beta_a$  between 10 and 20 K and a change in anisotropy from  $\beta_c/\beta_a < 2$  below 10 K to  $\beta_c/\beta_a \sim 10$  above 20 K, nevertheless, suggest that valence changes occur away from zero temperature. The temperature dependences of the CDW and SDW intensities and resistivity all show changes in this temperature range, the origin of which remains an open question.

Without magnetic order, a non-Kramers  $U^{4+}$  doublet ground state can form a two-channel Kondo state (44) (2CK) giving an MFL. Indeed, the calculated 2CK heat capacity (45, 46) scaled to the lattice density of  $\text{UAu}_2$  can reproduce the measured low-temperature heat capacity well (*SI Appendix, Fig. S15A*). The zero-temperature residual entropy  $0.5R \log(2)$  inherent in the 2CK state is, however, released on a temperature scale  $T_s$  when the degeneracy of the two channels is broken. The degeneracy is broken by an effective field (47) coming from both magnetic order and an applied field. A field of a tesla would give an easily visible increase of  $C/T$  (a detailed calculation is given in *SI Appendix*). Such an increase is not seen experimentally, implying that a uniform 2CK does not provide a straightforward explanation for our findings. We now examine whether the entropy release due to the magnetic order itself may result in an MFL.

The incommensurate nature of the modulated order means that there will be some ions that are located close to nodes of the total effective field comprising the sum of the field due to the modulated order and applied field. The two-channel Kondo analysis could still apply for these sites. For the sample as a whole, incommensurate order will result in a distribution of temperature scales  $T_s$  over which the 2CK residual entropy is released, with  $T_s$  extending down to zero temperature at the nodes. An MFL would result if the distribution of  $T_s$  values was constant as  $T_s \rightarrow 0$  or more precisely, constant to below the lowest temperature measured (*SI Appendix, Fig. S15B*). This idea is similar to one used to explain an MFL and linear in temperature resistivity in  $\text{Th}_{0.93}\text{U}_{0.07}\text{Ru}_2\text{Si}_2$  (48), based on a distribution of single-channel Kondo temperatures (19, 49) (in that case, the distribution was attributed to chemical disorder). We now briefly consider the distribution of  $T_s$  predicted theoretically. In the 2CK model,  $T_s$  is proportional to the square of the difference of the coupling strength for the two screening channels. For an isolated ion and no order, this results in  $T_s \propto H^2$ , where  $H$  is the magnetic field (47). This relation and a sinusoidal spatial variation for  $H$  due to magnetic order do not give the required flat distribution of  $T_s$  ( $T_s \propto H$  is required for this). A related problem was encountered when trying to explain the field dependence of the susceptibility and  $C/T$  in  $\text{Th}_{0.93}\text{U}_{0.07}\text{Ru}_2\text{Si}_2$  starting from the 2CK model. To get  $T_s \propto H$  for  $\text{Th}_{0.93}\text{U}_{0.07}\text{Ru}_2\text{Si}_2$ , models start from more complex crystal field schemes such as the accidental degeneracy of two singlets (50) or a combination of a non-Kramers doublet and two singlet levels (51, 52). These models move the sweet spot field at which the balanced 2CK response occurs from zero field to a finite field. The field distribution from the incommensurate order plus an applied field could continue to encompass the sweet spot over a wide range of applied fields. This would naturally explain the resilience of the MFL in an applied field. Also, since there is no longer a continuous field distribution in the  $F$  state, which is not modulated, this would also naturally account for the disappearance of the MFL. None of the above analyses consider coherence

between Kondo sites, which is a formidable theoretical challenge but essential to explain, for example, the behavior of the electrical resistivity.

## Conclusions

Although its crystal structure is incredibly simple,  $\text{UAu}_2$  has very unusual properties. The triangular lattice is a well-known source of magnetic frustration, and  $\text{UAu}_2$ 's Néel temperature is indeed less than the magnitude of its Curie–Weiss temperature (*SI Appendix*), consistent with a modest suppression of the ordering temperature due to frustration. The low-temperature magnetic structure we report is unique to  $\text{UAu}_2$ , but we have shown that it can be accounted for in a straightforward way. Frustration in this case resists the tendency for the modulation to square up as the temperature is reduced, so that other mechanisms that stabilize or quench the remaining fluctuating moments, such as Kondo screening, have an increased opportunity to play a role. At temperatures well below  $T_N$ , we found an NFL heat capacity that is surprisingly robust in magnetic field. Frustration and potential valence fluctuations invite comparisons with the NFL in  $\beta\text{-YbAlB}_4$  (12); however, the presence of magnetic ordering and robustness in magnetic field clearly distinguish  $\text{UAu}_2$  from  $\beta\text{-YbAlB}_4$ . Additionally, below  $T_N$ , a charge modulation was detected that is locked to the magnetic order but cannot be explained by simple magnetostriction. The intensity of charge modulation increases dramatically at low temperatures mirroring the NFL  $C/T$ , suggesting that these two features may be related. Charge transfer connected with the Anderson impurity description of Kondo physics is well established theoretically (53, 54) but has not, as far as we are aware, been observed experimentally in bulk materials. The incommensurate long-period nature of the magnetic order in  $\text{UAu}_2$ , however, means that this transfer may be observed in our case via diffraction, which coherently amplifies the signal, affording a possible explanation of the CDW we observe. The lack of saturation of the charge signal with decreasing temperature is then direct evidence for a range of Kondo scales  $T_s$ , extending to zero temperature, that would also explain  $C/T \sim \log(T)$ . The range is inherent to the modulated magnetism and does not necessarily require chemical disorder. While encouraging, this analysis does not include the coherence between Kondo sites and requires further development to account for the actual distribution of  $T_s$ . Our findings show that  $\text{UAu}_2$  forms an unusually robust NFL state in a clean material with a high residual resistivity ratio that is not anchored to a QCP. The simplicity of the material makes it more amenable to study than other 3D systems such as NFL states in high- $T_c$  superconductors, where QCPs are also present, and  $\text{MnSi}$ , where a robust NFL state is only attained at high pressure.

## Materials and Methods

Samples of  $\text{UAu}_2$  were obtained by the Czochralski method with a rotating tungsten seed from a radio frequency–levitated stoichiometric molten mixture of electrotransported depleted uranium (Ames Laboratories) and high-purity gold (99.999% Au; Alfa Aesar) contained by a water-cooled high-conductivity copper crucible under a purified argon atmosphere. Single crystalline grains within the sample were identified with Laue X-ray diffraction and cut with a spark eroder. Measurements of resistivity were performed by the standard four-point method on a Cryogenics Ltd closed cycle refrigerator (2 to 300 K) and Cryogenics Ltd/Leiden dilution refrigerator (0.05 and 1.4 K). A Quantum Design magnetic property measurement system Magnetometer was used to measure magnetization in fields up to 7 T, and a physical property measurement system was used to measure heat capacity above 500 mK (Fig. 3). Heat capacity measurements in Fig. 4 were performed by the relaxation method in a dilution refrigerator. Time-of-flight neutron diffraction data were taken on the WISH time-of-flight diffractometer at ISIS, Rutherford Appleton Lab, United Kingdom on both powder and single crystals. Resonant and nonresonant X-ray measurements were made at the UK Materials Science facility bending magnet 28 beamline at the European Synchrotron Radiation Facility, Grenoble, France. Further details on the experimental methods and materials are given in the *SI Appendix*.

**Data Availability.** The dataset has been deposited in the Edinburgh DataShare digital repository (<https://doi.org/10.7488/ds/3133>).

**ACKNOWLEDGMENTS.** We acknowledge support from UK Engineering and Physical Sciences Research Council Grants EP/P013686/1 and EP/R013004/1.

1. A. J. Schofield, Non-Fermi liquids. *Contemp. Phys.* **40**, 95–115 (1999).
2. P. Coleman, C. Pépin, Q. Si, R. Ramazashvili, How do Fermi liquids get heavy and die? *J. Phys. Condens. Matter* **13**, R723–R738 (2001).
3. B. Keimer, S. A. Kivelson, M. R. Norman, S. Uchida, J. Zaanen, From quantum matter to high-temperature superconductivity in copper oxides. *Nature* **518**, 179–186 (2015).
4. B. Michon *et al.*, Thermodynamic signatures of quantum criticality in cuprate superconductors. *Nature* **567**, 218–222 (2019).
5. S. D. Chen *et al.*, Incoherent strange metal sharply bounded by a critical doping in Bi2212. *Science* **366**, 1099–1102 (2019).
6. P. Gegenwart, Q. Si, F. Steglich, Quantum criticality in heavy-Fermion metals. *Nat. Phys.* **4**, 186–197 (2008).
7. M. Vojta, Frustration and quantum criticality. *Rep. Prog. Phys.* **81**, 064501 (2018).
8. C. Pfleiderer, S. R. Julian, G. G. Lonzarich, Non-Fermi-liquid nature of the normal state of itinerant-electron ferromagnets. *Nature* **414**, 427–430 (2001).
9. N. Doiron-Leyraud *et al.*, Fermi-liquid breakdown in the paramagnetic phase of a pure metal. *Nature* **425**, 595–599 (2003).
10. C. Pfleiderer *et al.*, Partial order in the non-Fermi-liquid phase of MnSi. *Nature* **427**, 227–231 (2004).
11. R. Ritz *et al.*, Formation of a topological non-Fermi liquid in MnSi. *Nature* **497**, 231–234 (2013).
12. Y. Masumoto *et al.*, Quantum criticality without tuning in the mixed valence compound  $\beta$ -YbAlB<sub>4</sub>. *Science* **331**, 316–319 (2011).
13. T. Tomita, K. Kuga, Y. Uwatoko, S. Nakatsui, High pressure measurements of the resistivity of  $\beta$ -YbAlB<sub>4</sub>. *J. Phys. Conf. Ser.* **592**, 012019 (2015).
14. R. M. Potok, I. G. Rau, H. Shtrikman, Y. Oreg, D. Goldhaber-Gordon, Observation of the two-channel Kondo effect. *Nature* **446**, 167–171 (2007).
15. T. Onimaru, H. Kusunose, Exotic quadrupolar phenomena in non-Kramers doublet systems: The cases of PrT<sub>2</sub>Zn<sub>20</sub> (T = Ir, Rh) and PrT<sub>2</sub>Al<sub>20</sub> (T = V, Ti). *J. Phys. Soc. Jpn.* **85**, 082002 (2016).
16. Y. Yamane *et al.*, Single-site non-Fermi-liquid behaviors in a diluted 4f<sup>2</sup> system Y<sub>1-x</sub>Pr<sub>x</sub>Ir<sub>2</sub>Zn<sub>20</sub>. *Phys. Rev. Lett.* **121**, 077206 (2018).
17. C. L. Seaman *et al.*, Evidence for non-Fermi liquid behavior in the Kondo alloy Y<sub>1-x</sub>U<sub>x</sub>Pd<sub>3</sub>. *Phys. Rev. Lett.* **67**, 2882–2885 (1991).
18. I. Affleck, A. W. W. Ludwig, Exact conformal-field-theory results on the multichannel Kondo effect: Single-fermion Green's function, self-energy, and resistivity. *Phys. Rev. B Condens. Matter* **48**, 7297–7321 (1993).
19. E. Miranda, V. Dobrosavljević, Disorder-driven non-Fermi liquid behaviour of correlated electrons. *Rep. Prog. Phys.* **68**, 2337–2408 (2005).
20. C. Pfleiderer, P. Böni, T. Keller, U. K. Rössler, A. Rosch, Non-Fermi liquid metal without quantum criticality. *Science* **316**, 1871–1874 (2007).
21. A. Miyake *et al.*, Pressure collapse of the magnetic ordering in MnSi via thermal expansion. *J. Phys. Soc. Jpn.* **78**, 044703 (2009).
22. M. Kontani *et al.*, Magnetic properties of binary and pseudobinary U-Au heavy Fermion systems. *J. Phys. Soc. Jpn.* **63**, 3421–3430 (1994).
23. R. Pöttgen, V. H. Tran, R. D. Hoffmann, D. Kaczorowski, R. Troc, Crystal structure and physical properties of UAuSi and UAu<sub>2</sub>. *J. Mater. Chem.* **6**, 429–434 (1996).
24. O. A. Starykh, Unusual ordered phases of highly frustrated magnets: A review. *Rep. Prog. Phys.* **78**, 052502 (2015).
25. Q. Sheng, C. L. Henley, Ordering due to disorder in a triangular Heisenberg antiferromagnet with exchange anisotropy. *J. Phys. Condens. Matter* **4**, 2937–2959 (1992).
26. M. Kuburagi, T. Tonegawa, J. Kanamori, Magnetic phase diagram for the triangular Ising lattice with antiferromagnetic nearest-neighbor and ferromagnetic next-nearest-neighbor interactions. *J. Phys. Soc. Jpn.* **51**, 3857–3867 (1982).
27. N. Todoroki, S. Miyashita, Ordered phases and phase transitions in the stacked triangular antiferromagnet CsCoCl<sub>3</sub> and CsCoBr<sub>3</sub>. *J. Phys. Soc. Jpn.* **73**, 412–416 (2004).
28. O. Koseki, F. Matsubara, Monte Carlo simulation of magnetic ordering of quasi-one dimensional Ising antiferromagnets CsCoBr<sub>3</sub> and CsCoCl<sub>3</sub>. *J. Phys. Soc. Jpn.* **69**, 1202–1206 (2000).
29. J. Villain, R. Bidaux, J. P. Carton, R. Conte, Order as an effect of disorder. *J. Phys.* **41**, 1263–1272 (1980).
30. D. Gignoux, D. Schmitt, "Magnetism of compounds of rare earths with non-magnetic metals" in *Handbook of Magnetic Materials*, K. H. J. Buschow, Ed. (Elsevier Science B.V., Amsterdam, the Netherlands, 1997), **vol. 10**, pp. 239–413.
31. S. Agrestini, C. Mazzoli, A. Bombardi, M. R. Lees, Incommensurate magnetic ground state revealed by resonant x-ray scattering in the frustrated spin system Ca<sub>3</sub>Co<sub>2</sub>O<sub>6</sub>. *Phys. Rev. B Condens. Matter Mater. Phys.* **77**, 140403 (2008).
32. S. Agrestini *et al.*, Slow magnetic order-order transition in the spin chain antiferromagnet Ca<sub>3</sub>Co<sub>2</sub>O<sub>6</sub>. *Phys. Rev. Lett.* **106**, 197204 (2011).
33. J. P. Hill, G. Helgesen, D. Gibbs, X-ray-scattering study of charge- and spin-density waves in chromium. *Phys. Rev. B Condens. Matter* **51**, 10336–10344 (1995).
34. V. J. Emery, S. A. Kivelson, J. M. Tranquada, Stripe phases in high-temperature superconductors. *Proc. Natl. Acad. Sci. U.S.A.* **96**, 8814–8817 (1999).
35. U. Walter, Treating crystal field parameters in lower than cubic symmetries. *J. Phys. Chem. Solids* **45**, 401–408 (1984).
36. A. J. Millis, Effect of a nonzero temperature on quantum critical points in itinerant fermion systems. *Phys. Rev. B Condens. Matter* **48**, 7183–7196 (1993).
37. H. v. Löhneysen, A. Rosch, M. Vojta, P. Wölfle, Fermi-liquid instabilities at magnetic quantum phase transitions. *Rev. Mod. Phys.* **79**, 1015–1075 (2007).
38. J. R. Schrieffer, Ward's identity and the suppression of spin fluctuation superconductivity. *J. Low Temp. Phys.* **99**, 397–402 (1995).
39. J. Custers *et al.*, Destruction of the Kondo effect in the cubic heavy-Fermion compound Ce<sub>3</sub>Pd<sub>20</sub>Si<sub>6</sub>. *Nat. Mater.* **11**, 189–194 (2012).
40. V. Martelli *et al.*, Sequential localization of a complex electron fluid. *Proc. Natl. Acad. Sci. U.S.A.* **116**, 17701–17706 (2019).
41. Q. Si, Global magnetic phase diagram and local quantum criticality in heavy Fermion metals. *Physica B* **378–380**, 23–27 (2006).
42. S. Doniach, The Kondo lattice and weak antiferromagnetism. *Phys. B+C* **91**, 231–234 (1977).
43. M. Dzero, M. R. Norman, I. Paul, C. Pépin, J. Schmalian, Quantum critical end point for the Kondo volume collapse model. *Phys. Rev. Lett.* **97**, 185701 (2006).
44. D. L. Cox, A. Zawadowski, Exotic Kondo effects in metals: Magnetic ions in a crystalline electric field and tunnelling centres. *Adv. Phys.* **47**, 599–942 (1998).
45. P. D. Sacramento, P. Schlottmann, Low-temperature properties of a two-level system interacting with conduction electrons: An application of the overcompensated multichannel Kondo model. *Phys. Rev. B Condens. Matter* **43**, 13294–13304 (1991).
46. Y. Shimizu, O. Sakai, S. Suzuki, Numerical renormalization group study of non-Fermi-liquid state on dilute uranium systems. *J. Phys. Soc. Jpn.* **67**, 2395–2407 (1998).
47. M. Fabrizio, A. O. Gogolin, P. Nozières, Crossover from non-Fermi-liquid to Fermi-liquid behavior in the two channel Kondo model with channel anisotropy. *Phys. Rev. Lett.* **74**, 4503–4506 (1995).
48. H. Amitsuka *et al.*, Non-Fermi-liquid behavior in R<sub>1-x</sub>U<sub>x</sub>Ru<sub>2</sub>Si<sub>2</sub> (R=Th, Y and La; x ≤ 0.07). *Physica B* **281–282**, 326–331 (2000).
49. E. Miranda, V. Dobrosavljević, G. Kotliar, Kondo disorder: A possible route towards non-Fermi-liquid behaviour. *J. Phys. Condens. Matter* **8**, 9871–9900 (1996).
50. A. I. Tóth, G. Kotliar, Hexadecapolar Kondo effect in URu<sub>2</sub>Si<sub>2</sub>? *Phys. Rev. Lett.* **107**, 266405 (2011).
51. S. Nishiyama, H. Matsuura, K. Miyake, Magnetically robust non-Fermi liquid behavior in heavy Fermion systems with f<sub>2</sub>-configuration: Competition between crystalline-electric-field and Kondo–Yosida singlets. *J. Phys. Soc. Jpn.* **79**, 104711 (2010).
52. S. Nishiyama, K. Miyake, Magnetic field effect on crossover temperature from non-Fermi liquid to Fermi liquid behavior in f<sub>2</sub>-impurity systems with crystalline-electric-field singlet state competing with Kondo–Yosida singlet state. *J. Phys. Soc. Jpn.* **80**, 124706 (2011).
53. C. J. Bolech, N. Andrei, Solution of the multichannel Anderson impurity model: Ground state and thermodynamics. *Phys. Rev. B Condens. Matter Mater. Phys.* **71**, 205104 (2005).
54. G. G. Blesio, L. O. Manuel, A. A. Aligia, P. Roura-Bas, Fully compensated Kondo effect for a two-channel spin S = 1 impurity. *Phys. Rev. B* **100**, 075434 (2019).